RSC Advances

ROYAL SOCIETY OF CHEMISTRY

www.rsc.org/advances

Hierarchical Peony-like $FeCO_3$ micro-flowers were selectively synthesized via a facile template-free hydrothermal process. Porous α-Fe_2O_3 derived from $FeCO_3$ maintained the original size and morphology of $FeCO_3$. To the best of our knowledge, this novel structure has not been reported. The excellent lithium storage properties of porous α-Fe_2O_3 micro- flowers were investigated.

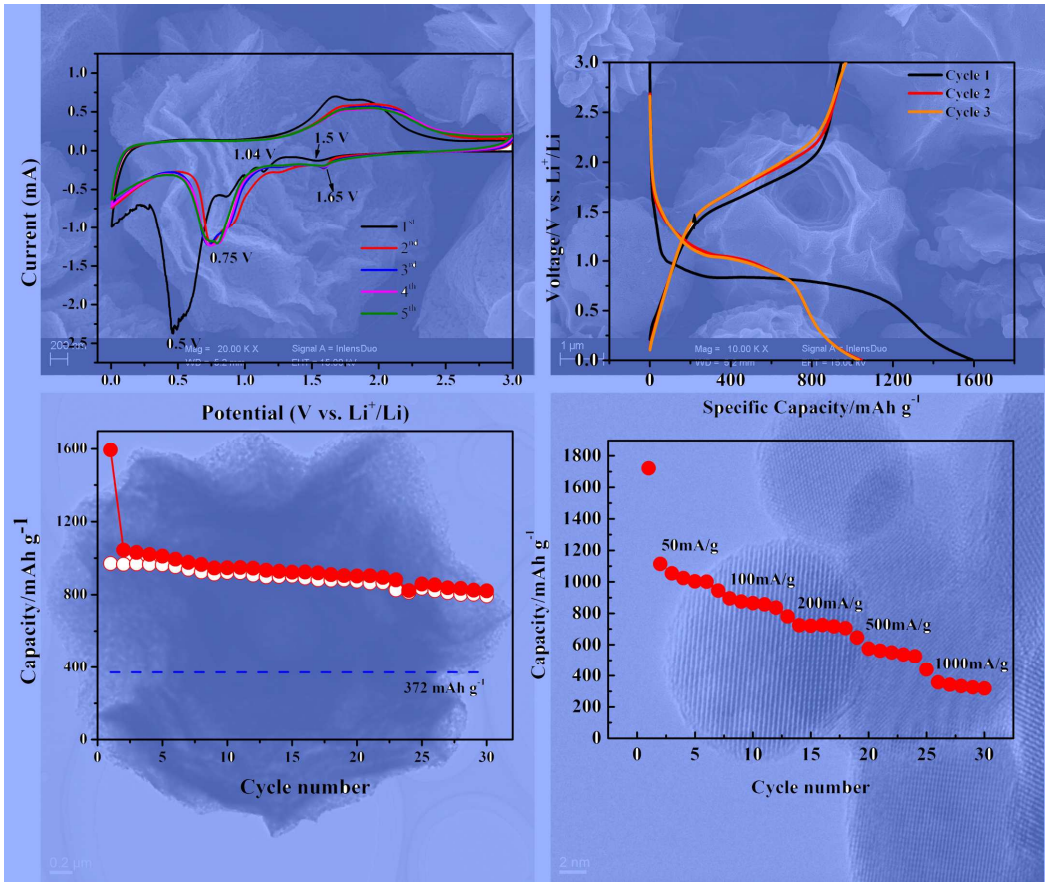

RSC Advances

RSCPublishing

ARTICLE

Porous Peony-like α-Fe_2O_3 Hierarchical Micro/nanostructures: Synthesis, Characterization and its Lithium Storage Properties

Cite this: DOI: 10.1039/x0xx00000x

Received 00th January 2014,
Accepted 00th January 2014

DOI: 10.1039/x0xx00000x

www.rsc.org/

Tao Yang, Yangai Liu*, Zhaohui Huang*, Qian Yang, Yongbo Chen, Meiling Hu, Ming Guan, Minghao Fang

In this work, hierarchical peony-like $FeCO_3$ structures with 3-5 μm diameter assembled from nanosheet layers were successfully prepared through a facile and well controlled hydrothermal method in the presence of an anionic surfactant sodium dodecyl sulfate (SDS). The factors influencing the morphology of hierarchical $FeCO_3$ structures were investigated. Hierarchical peony-like α-Fe_2O_3 structures assembled from nanoparticles were also fabricated by a thermal treatment of the as-obtained $FeCO_3$ at 700 °C for 3 h in air. Tested as anode materials of Li-ion batteries, the hierarchical porous peony-like α-Fe_2O_3 structures exhibited an excellent reversible capacity of 1721 mA h g^{-1} at a current density of 50 mA g^{-1} and a high cyclic stability at 100 mA h g^{-1} over 30 cycles. These results demonstrate the hierarchical porous α-Fe_2O_3 is a promising anode candidate for lithium ion batteries.

Introduction

Recently, lithium ion batteries (LIBs), as an important energy storage device, have trigger enormous attention in various fields such as electric vehicles (EV) and hybrid electric vehicles due to their high energy density and long cycle life, as well as excellent safety.[1-7] However, the commercially utilized graphite anode with relatively limited specific capacity (372 mA h g^{-1}) and low power density cannot meet the fast-growing demand of applications in high capacity and energy devices. Over the last several decades, driven by the increasing demand in electric vehicle and hybrid electric vehicle, considerable efforts have been devoted to explore novel anode materials with high performances to substitute for conventional graphite for LIBs.[8, 9] Among various anode materials, α-Fe_2O_3 is considered as the dominant anode material owing to its low toxicity, high availability and high theoretical specific capacity (1007 mAh g^{-1}), which is almost three times larger than that of conventional graphite.[10-12] But the practical application of α-Fe_2O_3 is limited by poor rate capability and unsatisfactory capacity retention resulting from serious volume changes during lithium insertion and extraction, which leads to electrode pulverization and irreversible capacity loss inevitably, and slow kinetics of electron and Li^+ diffusion.[11] One generally expressed strategy to alleviate these problems is to tailor special materials with micro-/nanostructures, to offer more active reaction sites and shorten Li^+ ions ion diffusion paths. In this regard, hierarchical three-dimensional ordered architectures assembled by one-dimensional or two-dimensional porous nanostructures is considered as an appealing and effective method to achieve excellent stability and remarkable rate capability for electrochemical applications because they can provide enlarged active surface areas and channels for Li^+ diffusion. [13-16]

Ferrous carbonate ($FeCO_3$) has received increasing attention since it can be served as a precursor to obtain porous α-Fe_2O_3.[17-20] It also has the potential using as an anode material in lithium storage applications. [21, 22] Due to the topotactic reaction between $FeCO_3$ and α-Fe_2O_3, the original morphology of the precursor can be easily maintained.[18] Meanwhile, α-Fe_2O_3 with porous structures will be acquired by properly controlling the thermal decomposition procedure where some pores will generated from crystals due to the release of CO_2 gas. However, nanosized or microsized/nanosized $FeCO_3$ structures are difficult to achieve on account of the fast precipitation rate during reaction process. Therefore, it is necessary to prepare these electrode materials with the reduced size or open channels in the precursor in order to improve the cyclic and rate performance of α-Fe_2O_3.

In this present work, hierarchical peony-like $FeCO_3$ microflowers (HFCFs) were prepared via a facile template-free hydrothermal method. Porous hematite microflowers with well-defined morphologies were synthesized by subsequently annealing the HFCFs in air at 700 °C for 3 h. This HFCFs exhibit a novel and unconventional morphology, which is different from that reported in the previous work. To our knowledge, there are no reports on the synthesis of this novel hierarchical peony-like $FeCO_3$ and porous α-Fe_2O_3 structures yet.

Experimental

Materials

Ferrous sulphate heptahydrate ($FeSO_4 \cdot 7H_2O$), ascorbic acid ($C_6H_8O_6$), urea ($CO(NH_2)_2$) , sodium dodecyl sulfate (SDS) were purchased from Beijing Chemistry Regent Company (Beijing, China). All chemical reagents were of analytical-grade and utilized as received without any further purification.

Synthesis

Hierarchical porous peony-like α-Fe_2O_3 structures were synthesized via a facile and well controlled hydrothermal method initially and a subsequent thermal treatment. In a typical preparation, 2 mmol of $FeSO_4 \cdot 7H_2O$, 3 mmol of $C_6H_8O_6$, 30 mmol of urea and 3 mmol of SDS were dissolved into 80 ml of distilled water, respectively, under continuous stirring for 30 min. After a transparent homogeneous solution was obtained, the solution was transferred into a sealed Teflon-lined autoclave and treated at a controlled temperature of (110±1) °C for 12 h in an electric oven. The precipitate was collected *via* centrifugation and then washed with distilled water and absolute ethanol for several times. Then the as-obtained sample was dried in a vacuum at 60 °C for 12 hours.

Materials Characterization

The crystallinity and phase of the as-prepared products were checked by X-ray diffraction (XRD) using Cu-Kα radiation. The scanning electron microscopy (SEM) images were recorded utilizing a MERLIN VP Compact field-emitting (FE) scanning electron microscope with an energy-dispersive X-ray spectrometer (EDS, Oxford Link ISIS). High-resolution transmission electron microscope images were taken by TEM (JEM-2010). Thermogravimetry analysis (TG) and differential scanning colorimeter (DSC, NETZSCH STA 449F3) were carried out to investigate the weight loss and transition energy of mixtures as a function of temperature at a heating rate of 5 °C/min. The X-ray photoelectron spectra (XPS) were collected on a Thermo Fisher ESCALAB 250 Xi XPS instrument (Thermo Fisher Scientific, Hudson, NH, USA).

Electrochemical Measurements

For the preparation of electrodes, the sample, super P, and polyvinylidene fluoride (PVDF) (75:15:10) were mixed and cast on a piece of copper foil current collector. The electrochemical tests were examined by assembling a coin-type electrochemical cell (2032-type), which was prepared with lithium foil as the reference and counter electrode and 1 M $LiPF_6$ dissolved in a mixture of ethylene carbonate (EC)/dimethyl carbonate (DMC)/diethyl carbonate (DEC) (1:1:1, in wt%) as the electrolyte. To cycle the coin-type electrochemical cells, the cells were discharged and charged at a constant current of 100 mAg^{-1} with cut-off voltage of 0.01 - 3.0 V (*vs* Li/Li^+). In the rate capability test, the current density was changed every five cycles according to the sequence of values: 50, 100, 200, 500 and 1000 mAg^{-1}. Cyclic voltammograms (CV) were carried out on a VMP3 electrochemical system (Princeton Applied Research) over the cut-off voltage of 0.01 - 3.0 V vs. Li/Li^+ at a scanning rate of 0.1 mV s^{-1}.

Results and discussion

The phase composition and purity of the as-prepared samples were investigated by X-ray diffraction (XRD), and the result of $FeCO_3$ precursors are given in Figure 1 (a). The diffraction peaks of the precursor can be assigned as the pure rhombohedral phase of $FeCO_3$ (JCPDS No. 29-0696) with a R-3c space group (a = 4.6935 Å, c = 15.386 Å), as shown in Fig. 1 (a). No other impurities were observed, indicating the high purity of the sample. Morphologies and sizes of the as-prepared samples were examined utilizing SEM. Figure 1 (b-f) shows the typical SEM image of the $FeCO_3$ sample which fabricated via hydrothermal reaction at 110 °C for 12 h.

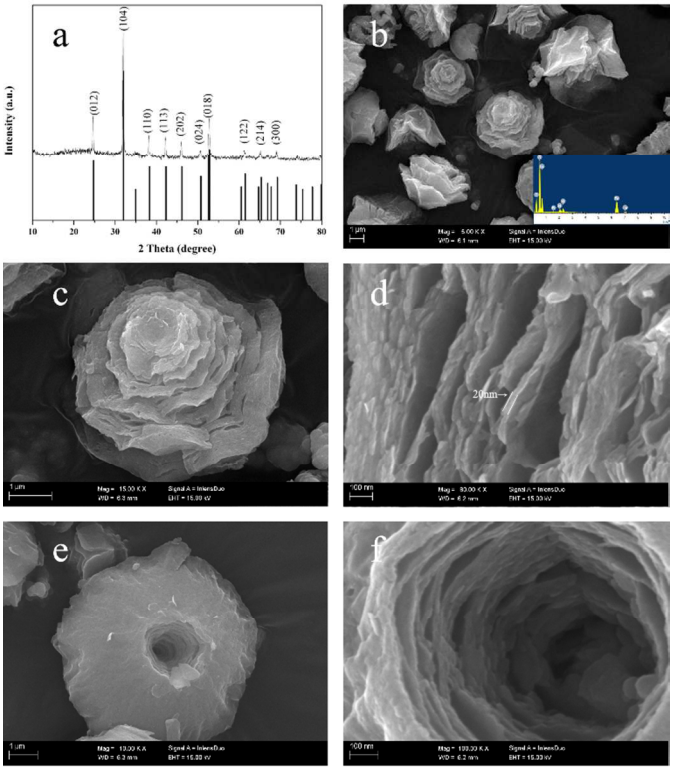

Figure 1. (a) The XRD pattern of the as-obtained $FeCO_3$ microflowers; (b) low-magnification FESEM images of $FeCO_3$ microstructures; (c-d) the top-view image and (e-f) the bottom-view of an individual architecture of $FeCO_3$.

It can be seen that the as-prepared $FeCO_3$ samples exhibit peony structure with a narrow size distribution. The average size of the peony-like structures was about 4 μm, as shown in Figure 1 (b). The corresponding EDS spectra (shown in the inset of Fig. 1b) reveal that the microspheres are composed of C, O and Fe originated from $FeCO_3$. XPS result of the as-synthesized $FeCO_3$ sample coincides well with that of the expressed standard as reported,[23] clearly indicating the original Fe 2p (i.e., $2p_{3/2}$ ~710.2 eV and $2p_{1/2}$ ~723.9 eV) peaks (Supplementary Information Figure S1). Closer observations are shown in Figure 1 (c-f), which illustrate the detailed structures of these flower-like morphologies. Each peony is

congregated regularly by layers of nanosheets with the thickness of about 20 nm as shown in the enlarged SEM image. It is worth noting that there is a hole with the diameter on the order of micrometer to submicrometer in the bottom of a single peony-like architecture of $FeCO_3$. The diameter of the hole reduce gradually as the peony aggregate completely. The effects of SDS on the morphology control were also investigated.

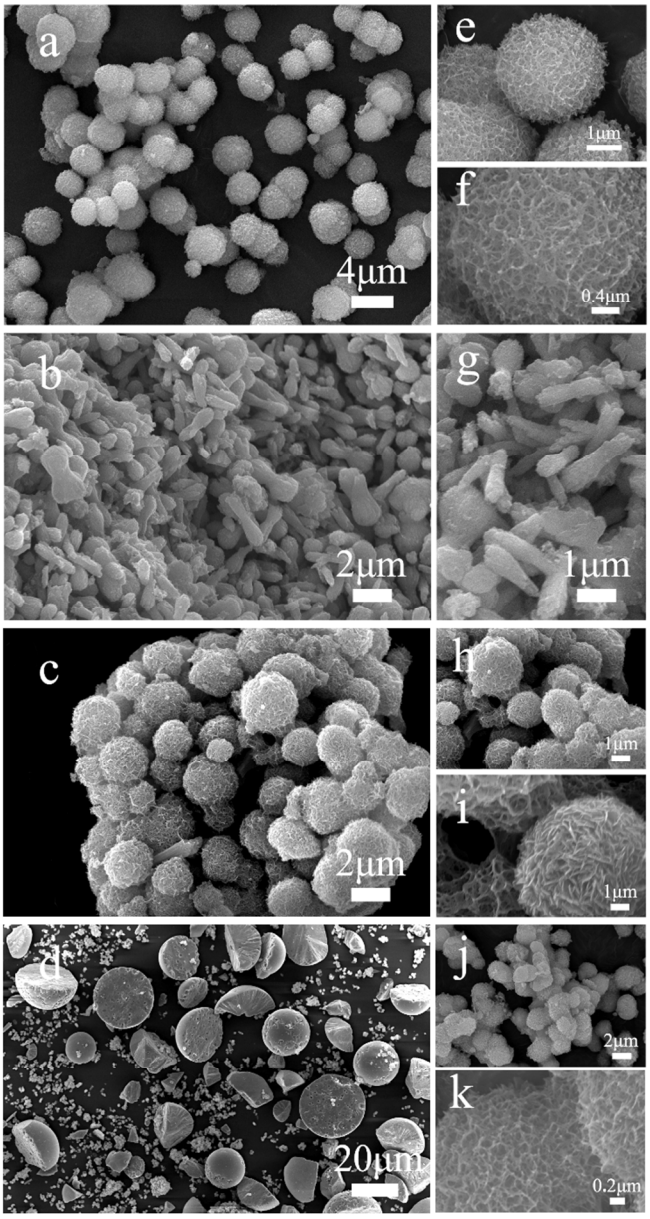

Figure 2. FESEM images of the products prepared by hydrothermal method at 110 °C at 12 h: (a, e, f) without surfactant; (b, g): with SDBS; (c, h, i): with CTAB; (d, j, k): with PVP.

As shown in Figure 2, when no SDS was added while other parameters were kept constant, the 3D porous spherical structures dominated in the full image (Figure 2a). A typical enlarged structure whose surfaces are covered by with dozens of nanowires is shown in the Figure 2a. These nanowires intertwined randomly to form the particular porous architectures. When SDBS was substituted for SDS, the products exhibited the 2D spindle-like structures with a wide size distribution Figure 2b. As the surfactant was replaced by cetyltrimethylammonium bromide (CTAB), the products possessed porous spheres assembled by numerous nanosheets with the diameter of about 2.5 μm (Figure 2c). It is remarkable that the products are composed of broken microspheres (size of 30-60 μm) and porous microspheres (size of 2-3μm) when the surfactant was changed to polyvinyl pyrrolidone (PVP, K30) (Figure 2d). The surface of broken microspheres was smooth while that of porous microspheres is net-like, which was also observed at the previous report.[18] Hence, it was concluded that both the selection of SDS and the amount used played critical roles in the fabrication of these 3D flowerlike structures.

Similarly to other metal carbonates, ferrous carbonate can decarbonise to form iron oxides with the porous morphology by a thermal treatment heating. The conversion process of ferrous carbonate precursor during calcination in air was studied via TG, as shown in Figure 3. Thermal decomposition in air leads to the conversion of $FeCO_3$ into iron oxide Fe_2O_3, depending upon the calcination temperature. The TGA analysis revealed that the initial weight loss of 6.11 wt % at 50~150 °C is due to the evaporation of absorbed water. The subsequent major weight loss ~35.75% found 150~500 °C is related to the decomposition of $FeCO_3$ into α-Fe_2O_3 and CO_2. Similar phenomenon have been detected in other carbonate. [24-25]

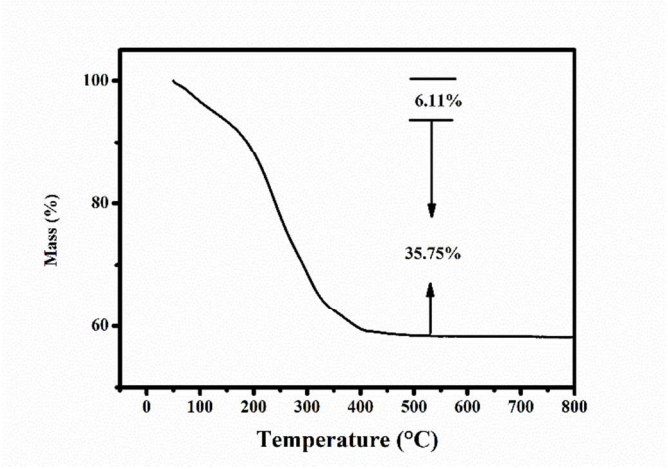

Figure 3. TG result of the $FeCO_3$ microflowers

The XRD patterns and morphologies of the products heated at different temperatures are shown in Supplementary Information (Figure S2 and S3). The original morphologies were maintained well and the pore was difficult to detect in the products calcined at 400 °C while more and more pores are observed in the as-calcined samples as increasing the heat treatment temperature. Therefore, the hierarchical porous α-Fe_2O_3 architecture can be obtained by calcination of the as-made $FeCO_3$ precursors. Figure 4a expressed the XRD pattern of the product obtained after anneal treatment at 700 °C in air for 3 h. All of the peaks can be indexed to the pure rhombohedral phase of α-Fe_2O_3 (JCPDS card #33-0664), indicating that the pure phase of α-Fe_2O_3 can be obtained by annealing the $FeCO_3$ precursors directly. In addition, the slightly broadened widths of these peaks indicated the nano-sized character of the 3D flowers,

in accordance with the magnified SEM result. The SEM images of the as-prepared α-Fe_2O_3 samples are also shown in Figure 4b-h. As a result, similar morphologies were detected as in the $FeCO_3$ precursors. What the different is that the layers are connected by numerous α-Fe_2O_3 nanoparticles with the diameter of less than 10 nm and its surface is porous. It has been well expressed that porous architectures will be beneficial for improving the electrochemical properties. The lattice fringe (Figure 4h) with an interplanar spacing of 0.27 nm was ascribed to the (104) plane of rhombohedral α-Fe_2O_3. The nitrogen adsorption and desorption measurements were carried out to estimate the Barrett-Joyner-Emmett-Teller (BET) surface area of the hierarchical peony-like α-Fe_2O_3 microflowers. The isotherm of the sample exhibits a hysteresis loop at the P/P_0 ranges of 0.6-1.0, indicating the presence of some amounts of mesoporosity (Supplementary Information Figure S4). The BET surface area of the hierarchical porous α-Fe_2O_3 microflowers was calculated as 12.95 m^2 g^{-1}.

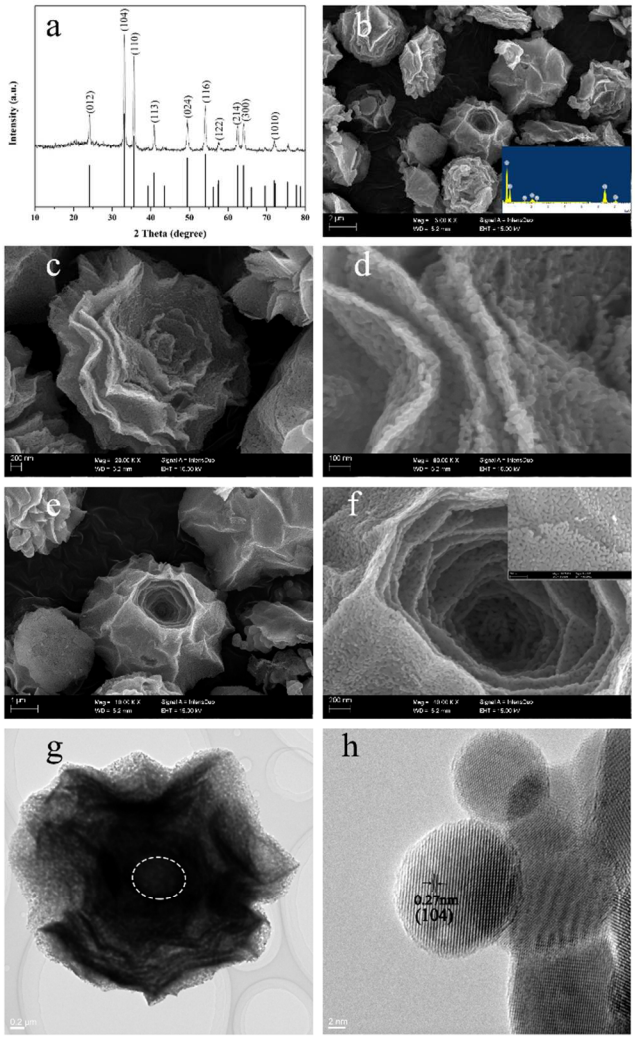

Figure 4. (a) The XRD pattern of the porous α-Fe_2O_3 microflowers; (b) low-magnification FESEM images of porous α-Fe_2O_3 microflowers; (c-d) the top-view image and (e-f) the bottom-view of an individual architecture of α-Fe_2O_3; (g-h) TEM and HR-TEM images of the as-calcined porous α-Fe_2O_3 microflower, respectively.

Inspired by the merits of porous structures as electrode materials in LIBs, the lithium storage properties of as-prepared porous hierarchical peony-like α-Fe_2O_3 structures were tested. The initial five CV curves of the electrodes made from as-prepared porous hierarchical peony-like α-Fe_2O_3 structures were recorded from 0.01 V to 3.0 V at a scan rate of 0.1 mV/s. In agreement with previous reports, there were two minuscule peaks at 1.04 V and 1.5 V in the cathodic sweep of the first cycle, both of which associate to the generation of hexagonal α-$Li_xFe_2O_3$ and phase transformation from α-$Li_xFe_2O_3$ to cubic $Li_2Fe_2O_3$. [26, 27] The cathodic peak at around 0.5 V corresponds to the electrolyte decomposition to form the solid electrolyte interface (SEI) and the complete conversion from Fe^{2+} to Fe^0. [28, 29] This lithium storage in the α-Fe_2O_3 sample proceed a multiple step reaction, which involve the phase transitions between hexagonal $LixFe_2O_3$, cubic $Li_2Fe_2O_3$ and Fe(0) summarized as follows:

$$\alpha\text{-}Fe_2O_3 + xLi^+ + xe^- \rightarrow \alpha\text{-}Li_xFe_2O_3$$

$$\alpha\text{-}Li_xFe_2O_3 + (2\text{-}x)Li^+ + (2\text{-}x)e^- \rightarrow Li_2Fe_2O_3 \text{ (cubic)}$$

$$Li_2Fe_2O_3 \text{ (cubic)} + 4Li^+ + 4e^- \rightarrow 2Fe^0 + 3Li_2O$$

$$\alpha\text{-}Fe_2O_3 + 6Li^+ + 6e^- \rightarrow 2Fe^0 + 3Li_2O$$

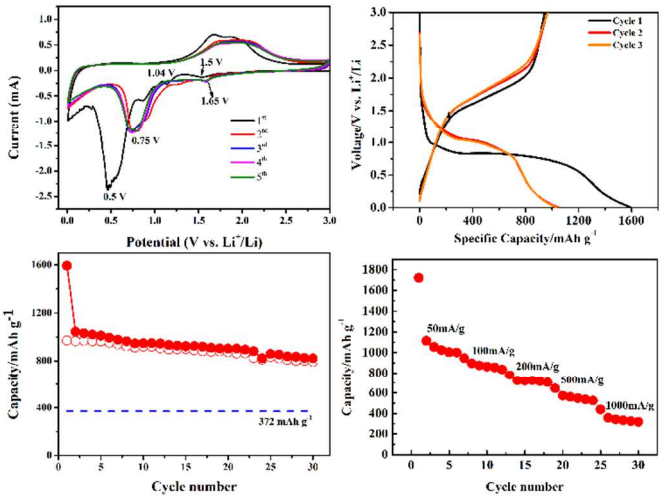

Figure 5. (a) Cyclic voltammetry curves of α-Fe_2O_3 samples measured between 0.01 and 3.0 V at the scan rate of 0.1 mV s^{-1}; (b) discharge and charge profiles of α-Fe_2O_3 samples cycled at the 1st, 2nd and 3rd between 0.01 V and 3.0 V; (c) galvanostatic cyclic performance of α-Fe_2O_3 samples at a current density of 100 mA g^{-1}; (d) Rate performance of α-Fe_2O_3 samples at variable C rates

The peaks disappear in the following cycles and change into a peak at 0.75 V, corresponding to the reversible lithium insertion and complete transition from FeO to Fe (0). On the other hand, the broad anodic peak at the potential of 1.6-1.8 V in the anodic sweep indicated the reversible oxidization of Fe (0) to Fe (III). [8, 30-32] All the peak intensity dropped in the following four cycles, which may be ascribed to the occurrence of some irreversible reactions with

formation of an SEI layer. [33, 34] Note that the CV curves exhibit a little change from the third to the fifth cycle, demonstrating the good reversibility of electrochemical reaction. Figure 5b shows the galvanostatic charge/discharge profile of the peony-like α-Fe_2O_3 electrode for the first, second and third cycling at the current density of 100 mA g^{-1}. In the initial discharge curve, a distinct voltage plateau is observed at around 0.75 V, and then shifts up to about 1.0 V where it remains stable for the following cycles. During the charge cycle, a plateau is detected about 1.6-1.8 V, which agrees well with the CV curves.

Figure 5c exhibits the discharge-charge cycling performance of the electrode at a current density of 100 mA g^{-1} for 30 cycles. The electrode exhibited an initial discharge capacity of 1593 mAh g^{-1}, with a reversible charge capacity of 971 mAh g^{-1}. The 40% initial irreversibility can be attributed to the irreversible formation of the solid electrolyte interface (SEI) layer or the decomposition of electrolyte, very common to most anode materials in lithium-ion battery. [33-35] In the subsequent cycle, the discharge and charge capacities of 1044 mAh g^{-1} and 966 mAh g^{-1} indicate a relatively high reversibility. The lithium storage capacity is firmly close to the theoretical value (~ 1007 mAh g^{-1}). The elevated storage capability, also was observed in other metal oxide nanostructures, was ascribed to the generation of LiOH and its subsequent reversible reaction with Li to form Li_2O and LiH. [33, 34] The reversible capacity remained 821 mA h g^{-1} with the capacity retention of 97% after 30 cycles, which about 2.2-fold higher than that of graphite. The electrochemical performance of the hierarchical peony-like α-Fe_2O_3 structures synthesized in this study and those of α-Fe_2O_3 with different morphologies reported in the literature are summarized in Table 1. It can be clearly found that the electrochemical performance of the hierarchical peony-like α-Fe_2O_3 structures is higher than the reported value of any additive-free α-Fe_2O_3 material in the literature. Therefore, it can be deduced that the hierarchical porous structures are conducive for the α-Fe_2O_3 anode material to achieve elevated properties.

To better understand the merits of this α-Fe_2O_3 electrode with special porous structures in improving lithium storage properties, the rate capacity of the α-Fe_2O_3 electrode were investigated (Fig. 5d). The α-Fe_2O_3 electrode exhibits a high reversible capacity of above 1721 mA h g^{-1} at a current density of 50 mA g^{-1}, which is one of the higher values for the reported iron oxide based anode materials [46-48]. As increasing the current density to 500 and 1000 mA g^{-1}, the specific capacity of the α-Fe_2O_3 electrode still maintains 561 and 357 mA h g^{-1}, indicating a high-rate performance.

Table 1 Comparison of the electrochemical performance of the α-Fe_2O_3 electrode with those of α-Fe_2O_3 with different morphology reported in the literature

Reference	Morphology	Initial capacity(mAh/g)	Capacity retention (mAh/g)/cycle number (current density (mA/g))
This work	hierarchial flowers	1593	821/30(100)
[36]	hierarchial flowers	1430	560/37(50)
[37]	nanospheres	1248.1	585.6/30(100)
[38]	flowers	974.43	548.47/30(100)
[39]	hollow spheres	1279	830/30(60)
[40]	nanopolyhedra	1660	668/20(50)
[41]	nanocapsules	1223	740/30(100)
[42]	nanoparticles	1010.9	186.9/80(60)
[43]	nanoparticles	1260	277.2/35(100)
[44]	nanoparticles	1085	350/50(50)
[45]	nanospindles	1135	151/10 (100)

Conclusions

In summary, a novel hierarchical peony-like $FeCO_3$ crystal was synthesized by a facile SDS-assisted hydrothermal method. The kind and the amount of surfactants played critical roles in the fabrication of these flowerlike structures. Then the porous hierarchical peony-like α-Fe_2O_3 was fabricated by a subsequent thermal calcination for use as a high-performance anode in

LIBs. Benefiting from the novel hierarchical peony-like structures aggregated by nanoparticles (less than 10 nm), the α-Fe_2O_3 electrode exhibited a high capacity, excellent cyclic stability and well rate performance. These results indicate a great potential of this electrode for high-performance lithium storage applications.

Acknowledgements

The authors acknowledge the financial support of the Fundamental Research Funds for the Central Universities (Grant No. 2012067), the Program for New Century Excellent Talents in University of Ministry of Education of China (Grant No. NCET-12-0951), the Science and Technology Innovation Funds for graduate students of China University of Geosciences (2012). T. Yang would like to acknowledge financial support from China Scholarship Council.

Notes and references

[a] School of Materials Science and Technology, China University of Geosciences (Beijing), Beijing 100083, P.R. China. *E-mail*: liuyang@cugb.edu.cn; huang118@cugb.edu.cn; *Tel*.: +86-010-82322186, *Fax*: +86-010-82322186.

Electronic Supplementary Information (ESI) available: [The XPS data of the as-synthesized $FeCO_3$ sample, XRD patterns and morphologies of the products heated at different temperature, BET nitrogen adsorption–desorption isotherms are provided.]. See DOI: 10.1039/b000000x/

1 K. Kang, Y.S. Meng, J. Breger, C.P. Grey and G. Ceder. Science, 2006, **311**, 977-980.

2 J. Chen and F. Cheng. Accounts chem. res., 2009, **42**, 713-723.

3 W. Wei, Z.H. Wang, Z. Liu, Y. Liu, L. He, D. Chen, A. Umar, L. Guo and J Li. J. Power Sources, 2013, **238**, 376-387.

4 Y. Yao, M. T. McDowell, I. Ryu, H. Wu, N. Liu, L.B. Hu, W. D. Nix, and Y. Cui. Nano Lett., 2011, **11**, 2949-2954.

5 X. Wang, X.-L. Wu, Y.-G. Guo, Y. T. Zhong, X.Q. Cao, Y. Ma, and J.N. Yao. Adv. Funct. Mater., 2010, **20**, 1680-1686.

6 W.M. Zhang, X.L. Wu, J.-S. Hu, Y.-G. Guo, and L.-J. Wan. Adv. Funct. Mater., 2008, **18**, 3941-3946.

7 L.F. Cui, Y. Yang, C.-M. Hsu and Yi Cui. Nano Lett., 2009, **9**, 3370-3374.

8 M. V. Reddy, T. Yu, C. H. Sow, Z. X. Shen, C. T. Lim, G. V. S. Rao and B. V. R. Chowdari. Adv. Funct. Mater., 2007, **17**, 2792-2799.

9 P. Poizot, S. Laruelle, S. Grugeon, L. Dupont and J-M. Tarascon. Nature, 2000, **407**, 496-499.

10 S. Xu, C. M. Hessel, H. Ren, R.B. Yu, Q. Jin, M. Yang, H.J. Zhao and D. Wang. Energ. Environmen. Sci., 2014, **7**, 632-637.

11 Y.-M. Lin, P. R. Abel, A. Heller, and C. B. Mullins. The J. Phys. Chem. Lett., 2011, **2**, 2885-2891.

12 J. Chen, L. Xu, W. Li and X. Gou. Adv. Mater., 2005, **17**, 582-586.

13 B. Zhang, Y. Zhang, Z.Z. Miao, T.X. Wua, Z.D. Zhang and X.G. Yang. J. Power Sources, 2014, **248**, 289-295.

14 V. Valtchev, and L. Tosheva. Chem. Rev., 2013, **113**, 6734-6760.

15 X.H. Rui, H.T. Tan, D.H. Sim, W.L. Liu, C. Xu, H. H. Hng, R. Yazami, T.M. Lim, Q.Y. Yan. J. Power Sources, 2013, **222**, 97-102.

16 H. Li, G. T. Fei, M. Fang, P. Cui, X. Guo, P. Yan, L.D. Zhang. Appl. Surf. Sci., 2011, **257**, 6527–6530.

17 G. Liu, Q. Deng, H.Q. Wang, Dickon H. L. Ng, M.G. Kong, W.P. Caia and G.Z. Wang. J. Mater. Chem., 2012, **22**, 9704-9713.

18 T. Yang, Z.H. Huang, Y.G. Liu, M.H. Fang, X. Ouyang and M.L. Hu. Ceram. Int., 2014, **40**, 11975-11983.

19 S.H. Xuan, L.Y. Hao, W.Q. Jiang, L. Song, Y. Hu, Z.Y. Chen, L.F. Fei, and T.W. Li. Cryst. Growth Des., 2007, **2**, 430-434.

20 X. Liu, H. Wang, C.H. Su, P.W. Zhang and J.B. Bai. J. Colloid Interf. Sci., 2010, **351**, 427-432.、

21 S. Zhao, Y. Yu, S.S. Wei, Y.X. Wang, C.H. Zhao, R. Liu and Q. Shen. J. Power Sources, 2014, **253**, 251-255.

22 Y.R. Zhong, L.W. Su, M. Yang, J.P. Wei, and Z. Zhou. ACS Appl. Mater. Interfaces, 2013, **5**, 11212-11217.

23 J.K. Heuer and J.F. Stubbins. Corros. Sci., 1999, **41**, 1231-1243.

24 X.Y. Jing, S.S. Song, J. Wang, L. Ge, S. Jamil, Q. Liu, T. Mann, Y. He, M.L. Zhang, H. Wei, L.H. Liu. Powder Technol., 2012, **217**, 624-628.

25 M. Y. Nassar, I. S. Ahmed. Mater. Res. Bull., 2012, **47**, 2638-2645.

26 J. Morales, L. Sanchez, F. Martin, F. Berry and X.L. Ren. J. Electrochem. Soc., 2005, **152**, A1748-A1754.

27 D. Larcher, D. Bonnin, R. Cortes, I. Rivals, L. Personnaz and J.-M. Tarascon. J. Electrochem. Soc., 2003, **150**, A1643-A1650.

28 G. Chen, R. Rodriguez, L. Fei, Y. Xu, S.G. Deng, S. Smirnov, H.M. Luo. J. Power Sources, 2014, **259**, 227-232.

29 S. Chaudhari and M. Srinivasan. J. Mater. Chem., 2012, **22**, 23049-23056.

30 Y. NuLi, R. Zeng, P. Zhang, Z.P. Guo and H.K. Liu. J. Power Sources, 2008, **184**, 456-461.

31 H.S. Kim, Y. Piao, S.H. Kang, T. Hyeon and Y.-E. Sung. Electrochem. Commun., 2010, **12**, 382-385.

32 H.D. Oh, S.W. Lee, S.-O. Kim, J.K. Lee. J. Power Sources, 2013, **244**, 575-580.

33 B. Wang, J.S. Chen, H.B. Wu, Z.Y. Wang, and X.W. (David) Lou. J. Am. Chem. Soc., 2011, **133**, 17146-17148.

34 Z.Y. Wang, D.Y. Luan, S. Madhavi, C. M. Lia and X.W. (David) Lou. Chem. Commun., 2011, **47**, 8061-8063.

35 X.D. Xu, R.G. Cao, S. Jeong , and J. Cho. Nano Lett., 2012, **12**, 4988-4991.

36 F. Han, D. Li , W.-C. Li, C. Lei, Q. Sun and A.-H. Lu. Adv. Funct. Mater., 2013, **23**, 1692-1700.

37 Y.Y. Hu, Z.G. Liu, K.-W. Nam, O. J. Borkiewicz, J. Cheng, X. Hua, M. T. Dunstan, X.Q. Yu, K. M. Wiaderek, L.-S. Du, K.W. Chapman, P. J. Chupas, X.-Q. Yang and C. P. Grey. Nat. Mater., 2013, **12**, 1130-1136.

38 W. Zhou, L.J. Lin, W.J. Wang, L.L. Zhang, Q. Wu, J.H. Li, and L. Guo. J. Phys. Chem. C, 2011, **115**, 7126-7133.

39 Y. NuLi, R. Zeng, P. Zhang, Z.P. Guo, H.K. Liu. J. Power Sources,

2008, **184**, 456-461.

40 S.Y. Zeng, K.B. Tang, T.W. Li, Z.H. Liang, D. Wang, Y.K. Wang, Y.X. Qi, and W.W. Zhou. J. Phys. Chem. C 2008, **112**, 4836-4843.

41 Z.C. Wu, K. Yu, S.D. Zhang, and Y. Xie. J. Phys. Chem. C, 2008, **112**, 11307-11313.

42 J.M. Ma, J.B. Lian, X.C. Duan, X.D. Liu, and W.J. Zheng. J. Phys. Chem. C, 2010, **114**, 10671-10676.

43 H.S. Kim, Y.Z. Piao, S. H. Kang, T. Hyeon, Y.-E. Sung. Electrochem. Commun., 2010, **12**, 382-385.

44 W.-J. Yu, P.-X. Hou, F. Li and C. Liu. J. Mater. Chem., 2012, **22**, 13756-13763.

45 H.-D. Oh, S.-W. Lee, S.O. Kim, J. K. Lee. J. Power Sources, 2013, **244**, 575-580.

46 G. Chen, R. Rodriguez, L. Fei, Y. Xua, S.G. Deng, S. Smirnov, H.M. Luo. J. Power Sources, 2014, **259**, 227-232.

47 S. Bai, S.Q. Chen, X.P. Shen, G.X. Zhu and G.X. Wang. RSC Advances, 2012, **2**, 10977-10984.

48 C. Shi, C. Cao, D. Wu, Y. Li, M. Wang and W. Mao. Mater. Lett., 2012, **83**, 35-38.

49 D. Su, H-S. Kim, W-S. Kim and G. Wang. Microporous Mesoporous Mater., 2012, **149**, 36-45.

50 S. Chaudharia and M. Srinivasan. J. Mater. Chem., 2012, **22**, 23049-23056.